Title

Membrane Curvature-sensing and Curvature-inducing Activity of Islet Amyloid Polypeptide and Its Implications for Membrane Disruption* ♦

Journal

Journal of Biological Chemistry, 290(43)

ISSN

0021-9258

Authors

Kegulian, Natalie C
Sankhagowit, Shalene
Apostolidou, Melania
et al.

Publication Date

2015-10-01

DOI

10.1074/jbc.m115.659797

Peer reviewed

THE JOURNAL OF BIOLOGICAL CHEMISTRY VOL. 290, NO. 43, pp. 25782–25793, October 23, 2015

Membrane Curvature-sensing and Curvature-inducing Activity of Islet Amyloid Polypeptide and Its Implications for Membrane Disruption*[S]◆

Received for publication, April 16, 2015, and in revised form, August 3, 2015 Published, JBC Papers in Press, August 17, 2015, DOI 10.1074/jbc.M115.659797

Natalie C. Kegulian[‡1], Shalene Sankhagowit[§], Melania Apostolidou[‡], Sajith A. Jayasinghe[‡2], Noah Malmstadt[§], Peter C. Butler[¶], and Ralf Langen[‡3]

From the [‡]Department of Biochemistry and Molecular Biology, Zilkha Neurogenetic Institute, Keck School of Medicine, University of Southern California, Los Angeles, California 90033, the [§]Mork Family Department of Chemical Engineering and Materials Science, University of Southern California, Los Angeles, California 90089, and the [¶]Larry Hillblom Islet Research Center, David Geffen School of Medicine at UCLA, Los Angeles, California 90095

Background: The mechanism behind diabetes-associated membrane damage by islet amyloid polypeptide (IAPP) is poorly understood.
Results: IAPP induces and senses membrane curvature under conditions associated with membrane damage and binds to mitochondrial cristae *in vivo*.
Conclusion: IAPP is a membrane-remodeling and curvature-sensing protein.
Significance: Aberrant membrane remodeling could inform disruption of membrane integrity in diabetes and perhaps other amyloid diseases.

Islet amyloid polypeptide (IAPP) is a 37-amino acid amyloid protein intimately associated with pancreatic islet β-cell dysfunction and death in type II diabetes. In this study, we combine spectroscopic methods and microscopy to investigate α-helical IAPP-membrane interactions. Using light scattering and fluorescence microscopy, we observe that larger vesicles become smaller upon treatment with human or rat IAPP. Electron microscopy shows the formation of various highly curved structures such as tubules or smaller vesicles in a membrane-remodeling process, and spectrofluorometric detection of vesicle leakage shows disruption of membrane integrity. This effect is stronger for human IAPP than for the less toxic rat IAPP. From CD spectra in the presence of different-sized vesicles, we also uncover the membrane curvature-sensing ability of IAPP and find that it transitions from inducing to sensing membrane curvature when lipid negative charge is decreased. Our *in vivo* EM images of immunogold-labeled rat IAPP and human IAPP show both forms to localize to mitochondrial cristae, which contain not only locally curved membranes but also phosphatidylethanolamine and cardiolipin, lipids with high spontaneous negative curvature. Disruption of membrane integrity by induction of membrane curvature could apply more broadly to other amyloid proteins and be responsible for membrane damage observed in other amyloid diseases as well.

Many neurodegenerative diseases, such as Alzheimer, Parkinson, and Huntington diseases, and type II diabetes are associated with amyloidogenic proteins (1). Islet amyloid polypeptide (IAPP[4] or amylin), a 37-residue peptide co-secreted with insulin (2, 3), is the principal component of islet amyloid commonly present in type II diabetes (4). Furthermore, numerous cell and animal studies support a causative role of human IAPP (hIAPP) in type II diabetes (5–7). As in the case of other amyloidogenic proteins (8–10), disruption of membrane integrity is thought to be one of the mechanisms by which IAPP can cause toxicity (5, 11, 12).

Different mechanisms have been proposed for IAPP-dependent membrane damage, with some of the more recent studies (13–15) illustrating IAPP-mediated membrane disruption to occur in two or possibly more (16) steps. In one model, hIAPP damages membranes at the amyloid fibril formation stage, such that hIAPP fibrils forming near the membrane extract lipid from the membrane as they grow; this lipid uptake process

* This work was supported, in whole or in part, by National Institutes of Health Grants G027936 and GM063915 (to R. L.) and 1R01GM093279 (to N. M.) and Grant DK-059579 from the NIDDK (to P. C. B.). This work was also supported by National Science Foundation Award CMMI-1068212 (to N. M.). The authors declare that they have no conflicts of interest with the contents of this article.
◆ This article was selected as a Paper of the Week.
[S] This article contains supplemental Videos S1 and S2.
[1] Supported by National Institutes of Health Predoctoral Training Grant 5T32GM067587-10.
[2] Present address: Dept. of Chemistry and Biochemistry, California State University, San Marcos, CA 92096.
[3] To whom correspondence should be addressed: Dept. of Biochemistry and Molecular Biology, Zilkha Neurogenetic Institute, 1501 San Pablo St., ZNI 119, Los Angeles, CA 90089-2821. Tel.: 323-442-1323; Fax: 323-442-4404; E-mail: langen@usc.edu.

[4] The abbreviations used are: IAPP, islet amyloid polypeptide; hIAPP, human IAPP; rIAPP, rat IAPP; ThT, thioflavin T; MLV, multilamellar vesicle; POPS, 1-palmitoyl-2-oleoyl-*sn*-glycero-3-[phospho-L-serine]; POPG, 1-palmitoyl-2-oleoyl-*sn*-glycero-3-[phospho-RAC-(1-glycerol)]; DOPG, 1,2-dioleoyl-*sn*-glycero-3-[phospho-rac-(1-glycerol)]; HFIP, hexafluoroisopropanol; ANTS, 8-aminonaphthalene-1,3,6-trisulfonic acid; DPX, *p*-xylene-bis(pyridinium bromide); Rh-PE, 1,2-dioleoyl-*sn*-glycero-3-phosphoethanolamine-*N*-[lissamine rhodamine B sulfonyl]; POPC, 1-palmitoyl-2-oleoyl-*sn*-glycero-3-phosphatidylcholine; LUV, large unilamellar vesicle; SUV, small unilamellar vesicle; NBD-PS, 1-palmitoyl-2-{12-[(7-nitro-2–1,3-benzoxadiazol-4-yl)-amino]dodecanoyl}-*sn*-glycero-3-phosphoserine; biotin-PE, 1,2-dipalmitoyl-*sn*-glycero-3-phosphoethanolamine-*N*-(cap biotinyl); GUV, giant unilamellar vesicle; MRE, mean residue ellipticity.

results in nonspecific rupturing and fragmentation of the membrane by the nascent fibrils (17, 18). However, rat IAPP (rIAPP), which does not readily form fibrils (19), has also been seen to cause membrane leakage *in vitro* (16) and confer some (albeit strongly reduced) cytotoxicity *in vivo* (12). Also, the nonamyloidogenic hIAPP(1–19) fragment as well as a number of nonamyloidogenic full-length variants of IAPP have been observed to cause leakage of synthetic membranes (13, 15, 20), and hIAPP(1–19) and rIAPP(1–19) can permeabilize pancreatic islet cell membranes (21). Therefore, fibril growth cannot be the sole mechanism involved. Other mechanisms have been suggested that are analogous to those utilized by antimicrobial peptides (22–24). Peptides that employ the detergent-like carpet mechanism cause widespread defects throughout the membrane surface in a nonspecific manner (25–28). Pore models, in contrast, entail monomers assembling to form a discrete oligomer in the membrane that acts as a pore with ion channel-like properties (29, 30) or, alternatively, peptides inducing the membrane to form a toroidal pore lined by its own phospholipids (31–33). Different studies have proposed a variety of mechanisms such as these for IAPP, including pore mechanisms (16, 34–38). Given the increasingly established bi- or multiphasicity of IAPP-mediated membrane damage (13–16), one or more of the above mechanisms could be part of an early step, with the later or latest step involving β-sheet fibril formation.

One possibility that remains unexplored is that IAPP induces membrane curvature as an α-helical wedge. Prior to forming β-sheet fibrils, IAPP is known to bind to negatively charged lipids and detergents using an amphipathic α-helical structure (39–43). Here, we hypothesize that the insertion of such a helical structure into negatively charged membranes might induce and/or sense membrane curvature. Other proteins that form membrane-bound amphipathic α-helices are known to induce membrane curvature by pushing phospholipid headgroups apart, thereby effectively acting as wedges. Examples include the H0 α-helices of N-BAR domain proteins such as amphiphysin and endophilin (44–51). In addition, α-synuclein binds to negatively charged membranes as an amphipathic α-helix that alone is sufficient to induce membrane curvature, or in other words to remodel liposomes into tubular structures, small, highly curved vesicles, or protein-lipid nanoparticles (52–55). Importantly, such membrane remodeling and induction of membrane curvature can cause disruption of membrane integrity (52). Furthermore, at presynaptic termini in transgenic mice, overexpressed human α-synuclein was associated with remodeling of organelle membranes into highly curved structures (56). We therefore tested whether some of the previously observed membrane-disrupting effects of IAPP might have been caused by induction of membrane curvature. Moreover, prior studies on membrane curvature-inducing proteins have shown that such proteins can also exhibit curvature-sensitive membrane binding under some conditions (44, 57–61). Inasmuch as sensing of membrane curvature could have implications for physiological and pathogenic recruitment of IAPP to membranes, we also investigated the curvature sensitivity of the IAPP-membrane interaction.

Using circular dichroism (CD), spectrophotometry, and fluorescence microscopy of GUVs, we find that α-helical IAPP converts large, negatively charged vesicles into much smaller structures. Dye leakage experiments indicate that this membrane remodeling coincides with significant disruption of membrane integrity, and electron microscopy reveals the IAPP-dependent formation of lipid tubules and smaller vesicles. By uncovering IAPP as a curvature inducer, we can correlate the previously discovered early phase of membrane leakage with the modulation of membrane architecture into highly curved structures. When using only weakly negatively charged membranes, we find that IAPP transitions from an inducer of membrane curvature to a sensor of membrane curvature. The induction or sensing of membrane curvature may impact IAPP's physiological and pathological functions and govern its membrane localization *in vivo*. In support of this notion, we show that IAPP preferentially localizes to mitochondria, where it interacts with cristae. Cristae are curved membrane structures rich in cardiolipin and phosphatidylethanolamine, lipids with pronounced negative spontaneous curvature.

Experimental Procedures

Materials—Synthetic hIAPP was obtained from Bachem (Torrance, CA), and synthetic rIAPP was from BiomerTech (Pleasanton, CA). 1-Palmitoyl-2-oleoyl-*sn*-glycero-3-phosphatidylcholine (POPC), 1-palmitoyl-2-oleoyl-*sn*-glycero-3-[phospho-L-serine] (POPS), 1-palmitoyl-2-oleoyl-*sn*-glycero-3-[phospho-RAC-(1-glycerol)] (POPG), 1,2-dioleoyl-*sn*-glycero-3-[phospho-RAC-(1-glycerol)] (DOPG), 1-palmitoyl-2-{12-[(7-nitro-2–1,3-benzoxadiazol-4-yl)amino]dodecanoyl}-*sn*-glycero-3-phosphoserine (NBD-PS), 1,2-dioleoyl-*sn*-glycero-3-phosphoethanolamine-*N*-[lissamine rhodamine B sulfonyl] (Rh-PE), and 1,2-dipalmitoyl-*sn*-glycero-3-phosphoethanolamine-*N*-(cap biotinyl) (biotin-PE) were obtained as solutions in chloroform from Avanti Polar Lipids, Inc. (Alabaster, AL). Hexafluoroisopropanol (HFIP), HEPES, thioflavin T (ThT), Triton X-100, and asolectin were obtained from Sigma; 8-aminonaphthalene-1,3,6-trisulfonic acid (ANTS), *p*-xylene-bis(pyridinium bromide) (DPX), and avidin were from Life Technologies, Inc.; guanidine hydrochloride was from Thermo Scientific; and uranyl acetate was from Electron Microscopy Sciences (EMS, Hatfield, PA). Polydimethylsiloxane was purchased from Dow Corning (Midland, MI).

Preparation of Peptides—hIAPP or rIAPP powder was initially dissolved in HFIP. To quantify peptide concentrations, a small amount of peptide was isolated; the HFIP was evaporated under a stream of nitrogen gas and replaced with 8 M guanidine HCl, and absorbance at 280 nm was measured. hIAPP in HFIP was then aliquoted, flash-frozen in liquid N_2, and lyophilized overnight. Immediately prior to each experiment, hIAPP was redissolved in 10 μl of deionized water containing 0.5% acetic acid, to which 40 μl of 110 mM HEPES, pH 7.4, was added. The resulting peptide solution was added to vesicles to a final peptide concentration of 25 μM (unless otherwise indicated). For rIAPP, HFIP was evaporated under a nitrogen stream, and the peptide was redissolved in 10 mM HEPES, pH 7.0, 50 mM KCl, or 10 mM sodium phosphate, pH 7.0, no salt. Immediately before each experiment, peptide solution was centrifuged in a tabletop Eppendorf 5415D centrifuge at 13,200 rpm for 10 min; the supernatant was taken, and the peptide concentration was determined using A_{280}. To perform the experiment, the appro-

priate amount of peptide was then added to vesicles to reach a final peptide concentration of 25 μM (unless otherwise indicated).

α-Synuclein was prepared as described previously (62). Briefly, the protein was expressed in *Escherichia coli* BL21 (DE3) pLysS cells (New England Biolabs, Inc.) and subsequently purified by boiling, acid precipitation, passage of the resulting supernatant through anion exchange columns, and elution with a 0–1.0 M NaCl gradient. Prior to use in clearance assays, α-synuclein was buffer-exchanged via PD-10 columns (GE Healthcare) into 10 mM HEPES, pH 7.0, 50 mM KCl.

Preparation of Phospholipid Vesicles—POPS and POPC in chloroform were mixed to obtain the desired lipid molar ratios. For these mixtures and for individual preparations of POPC, POPS, POPG, or DOPG, the chloroform was evaporated under a stream of nitrogen, and the resulting lipid mixture was dried in a vacuum desiccator overnight. For lipid clearance and electron microscopy experiments, dried lipid mixtures were rehydrated in 10 mM HEPES, 50 mM KCl, pH 7.0, and used as the resulting multilamellar vesicles (MLVs) without further manipulation.

For leakage assays, large unilamellar vesicles (LUVs) with a diameter of 100 nm were prepared. First, lipids were rehydrated in 10 mM HEPES, pH 7.0, 2.4 mM KCl, 1 mM EDTA, 3 mM sodium azide, 9 mM ANTS, and 25 mM DPX. This resuspension was subjected to 10 cycles of freeze/thaw, followed by at least 21 extrusions through two 100-nm-cutoff polycarbonate membranes (Avanti). Unencapsulated ANTS and DPX were removed by gel filtration using Sephadex G-100 medium (GE Healthcare), eluting the LUVs in 10 mM HEPES, pH 7.0, 50 mM KCl, 1 mM EDTA, and 3 mM sodium azide.

For *in vitro* curvature sensitivity measurements, lipids were rehydrated in 10 mM sodium phosphate, pH 7.0, no salt. 100-nm LUVs were prepared by freeze/thawing and extruding the vesicle suspension as described above. SUVs were prepared by bath-sonicating the suspension, then centrifuging it in an Optima TLX Ultracentrifuge (Beckman Coulter, Inc.) at 60,000 rpm for 1 h using an Optima TLA-100.3 fixed-angle rotor (Beckman Coulter), and collecting the supernatant.

Preparation of giant unilamellar vesicles (GUVs) was modified from a previous method (63). Briefly, the lipid mixture dissolved in chloroform was dried on an indium-tin oxide-coated glass slide (Delta Technologies, Loveland, CO) and stored under vacuum overnight. The resulting lipid film was hydrated with the addition of 10 mM HEPES, pH 7.0, 100 mM sucrose to the volume enclosed by two indium-tin oxide-coated slides and a 2.5-mm-thick silicon spacer. The GUVs were formed at room temperature (~23 °C) by applying a 1.5-V alternating current field with a frequency of 10 Hz for 1 h.

Vesicle Clearance Assay—Clearance of MLVs was monitored by measuring change in light scattering as a function of time at a wavelength of 500 nm and a slit width of 2 nm in a Jasco V-550 spectrophotometer. hIAPP, rIAPP, α-synuclein, or buffer as a control was added to vesicles in a quartz cuvette. IAPP was added to a final protein/phospholipid molar ratio of 1:20, except where otherwise indicated. α-Synuclein was added at a lower molar concentration to a final protein/lipid molar ratio of 1:74, to match the mass to lipid ratio used in the IAPP experiments. Each experiment was performed at least in triplicate. Data were normalized by setting initial values to 1 and thereby plotting the fraction of remaining light scattering as A_{500} at each time point. Data for the concentration dependence test (Fig. 1*E*) were scaled by dividing the clearance value (defined as the difference between 1 and the normalized A_{500}) for each sample at 100 s by the highest clearance value across all samples at 100 s. As a result, the lowest clearance value was set to 0 and the highest was set to 1.

CD—Measurements were taken using a Jasco J-810 spectropolarimeter in a 1-mm quartz cell every 0.5 nm at a 50-nm/min scan rate and a response time of 1 s. For each spectral measurement performed in parallel to the clearance assay, eight scans were averaged, and the appropriate background was subtracted; then the spectrum was smoothed by the Savitsky-Golay method. For CD spectra measured to determine curvature sensitivity, 16 scans were averaged, and the appropriate background was subtracted, and experiments were performed in 10 mM sodium phosphate, pH 7.0, no salt. In all cases, values were normalized to obtain mean residue ellipticity (MRE).

ThT Assays—To monitor possible fibril formation from peptides, ThT fluorescence assays were also performed in parallel using 25 μM ThT in the sample. Emission intensities at 482 nm were measured as a function of time with excitation at 450 nm, excitation and emission slit widths of 1 and 10 nm, respectively, and a response time of 1 s. Measurements were taken using a Jasco FP-6500 spectrofluorometer and normalized to the maximal fluorescence values.

Fluorescence Microscopy—The NBD-PS and Rh-PE-labeled GUVs were observed with confocal fluorescence microscopy on a Nikon TI-E inverted microscope, using illumination provided by 50-milliwatt solid-state 491- and 561-nm lasers for the dyes and capturing fluorescent emissions at 525 and 595 nm, respectively. To minimize volumes used during observations of GUVs, an ~4.6-mm-thick polydimethylsiloxane sheet with a 6-mm-diameter cylindrical hole was attached to the coverslip to form an ~130-μl observation well. The 0.3% biotin-PE GUVs were immobilized with avidin-biotin tethers to a supported lipid bilayer on the glass coverslip surface. The supported bilayer was prepared by rupturing 85:15 (molar) asolectin/biotin-PE LUVs onto glass. These LUVs were formed by 30-min sonication at 30 °C of overnight vacuum-dried lipid film hydrated to a 2 mg/ml concentration with 10 mM HEPES, pH 7.0, 50 mM KCl. The LUVs were then filtered through the 0.45-μm cellulose membrane of a syringe filter (VWR International, Radnor, PA). This LUV solution was deposited onto the glass surface, left for 30 min, and rinsed via pipetting with 10 mM HEPES, pH 7.0, no salt. Next, a 1 mg/ml avidin solution in water was added and left for 15 min and was followed by the same rinsing procedure but with the 10 mM HEPES, pH 7.0, 50 mM KCl. The GUVs were added to the observation well and allowed 10 min to sediment to the coverslip surface, after which excess vesicles were removed to prevent the peptides from acting on floating, unobservable vesicles prior to reaching those in focus. The resulting GUV lipid molar concentration was estimated to be on the order of 2.5 to 5 times the final concentration of peptide used in each experiment.

Leakage Assay—IAPP was added to LUVs at a protein/phospholipid molar ratio of 1:20, except where otherwise indicated.

Release of ANTS and its quencher DPX was gauged as an increase in ANTS fluorescence intensity as a function of time. Excitation and emission wavelengths were set at 380 and 520 nm with slits of 1 and 12 nm, respectively, and a response time of 1 s. One hundred percent leakage was attained using a final concentration of 0.04% Triton X-100, and all data were normalized to fluorescence intensity at this amount. Data for the concentration dependence test (Fig. 1*E*) were scaled by dividing the normalized leakage value for each sample at 100 s by the highest normalized leakage value across all samples at 100 s. As a result, the lowest leakage value is set to 0 and the highest to 1.

Electron Microscopy (EM) of Vesicles—Samples were deposited as 10-μl droplets on parafilm and carbon-coated Formvar films mounted on copper grids (EMS) floated on top for 5 min. Then, after blotting the excess liquid with filter paper, grids were floated on 10-μl droplets of 1% uranyl acetate for 1 min for negative staining. Microscopy was performed using a JEOL 1400 transmission electron microscope accelerated to 100 kV. To build size distribution histograms, MLVs composed of POPS were initially extruded to 1 μm in diameter, and an arbitrarily chosen quadrant was sampled for each of a series of images taken of POPS alone, POPS with hIAPP, and POPS with rIAPP; quadrants chosen throughout each series were those at the same placement as the first arbitrarily chosen quadrant for that series. Subsequently, the vesicles within the chosen quadrant for each series were counted for every image in that series and then categorized by size.

EM of Pancreatic Cells—With Animal Use and Care Committee approval, the whole pancreas was removed from a wild type female FVB mouse after euthanasia, and tissue was minced in Trump's solution at 4 °C, fixed for 3 h, and then transferred to 0.1 M phosphate buffer. With Institutional Review Board approval, human insulinoma tissue previously obtained at surgery as described (64) was also minced immediately in Trump's solution and then postfixed in 1% osmium tetroxide. Samples from both the mouse pancreas and human insulinoma were then dehydrated in increasing concentrations of acetone, embedded in Quetol resin, and polymerized at 40 °C, and 80-nm sections were placed on nickel grids for immunogold labeling of IAPP as described previously (64).

Results

IAPP Transforms Negatively Charged Vesicles into Smaller Structures—To test whether IAPP can remodel membranes, we added human or rat IAPP to MLVs made up of POPS, a negatively charged phospholipid, and monitored the change in light scattering by measuring A_{500} over time, as described previously for α-synuclein (52). Fig. 1*A* shows that hIAPP and, to a lesser extent, rIAPP cleared scattering by POPS MLVs, indicating their ability to transmute large vesicles into smaller entities. We performed the same assay using buffer alone as a negative control or α-synuclein, which is known to cause clearance of phosphatidylglycerol MLVs (52, 54). Buffer induced no difference in light scattering, whereas α-synuclein caused some POPS clearance, although less so than either type of IAPP (Fig. 1*A*). Vesicles made up entirely of the zwitterionic phospholipid POPC showed no clearance upon addition of any peptide or buffer control (Fig. 1, *B* and *C*). These results suggest that the electrostatic interactions between IAPP and the membrane lead to loss of scattering by vesicles. To more systematically investigate how the change in scattering depends on the presence of negatively charged POPS, we reduced the percentage of POPS in the vesicle composition by replacing it with POPC. We found that the less POPS the vesicle membranes contained, the less clearance was observed (Fig. 1*C*). hIAPP was generally more potent than rIAPP at reducing the scattering, and this difference was particularly pronounced at 33% POPS. Readings shown were collected before the onset of aggregation, as illustrated by the example of CD spectra measured in the presence of 100% POPS (Fig. 1*D*), which after 1 h of clearance contained negative peaks at 208 and 222 nm, indicating α-helical, as opposed to β-sheet, structure.

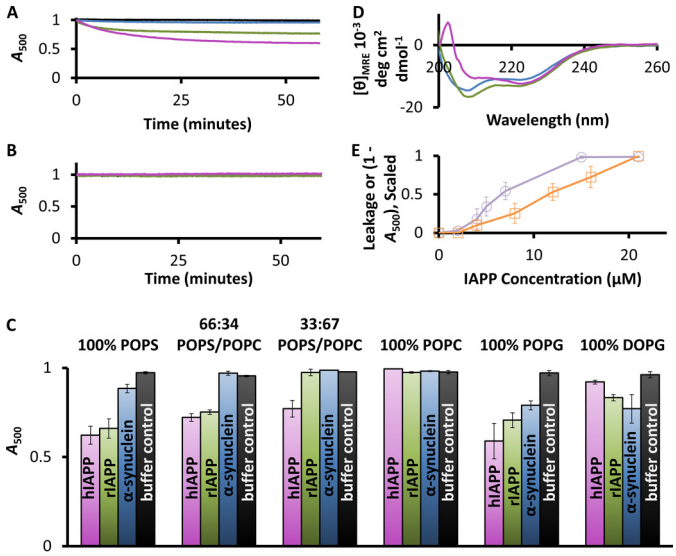

FIGURE 1. **Light scattering of MLVs.** Changes in light scattering upon addition of hIAPP (*magenta*), rIAPP (*green*), α-synuclein (*blue*), or buffer (*black*) were determined from the absorbance at 500 nm. Clearance curves of 100% POPS (*A*) or 100% POPC (*B*) were measured in the presence of each protein or buffer control. *C,* lowest light scattering reading within the 1st h of clearance for MLVs of the indicated phospholipid compositions. *Error bars* represent standard error; $N \geq 3$. *D,* CD spectra of hIAPP, rIAPP, and α-synuclein mixed with 100% POPS. *E,* light scattering loss (*orange*) and vesicle leakage (*light purple*) of 66:34 POPS/POPC MLVs or LUVs, respectively, at 100 s upon addition of hIAPP at the indicated concentrations. Phospholipid concentration is 500 μM; IAPP concentration is 25 μM except in *E* as indicated, and α-synuclein concentration is 6.74 μM, to match the IAPP concentration of 25 μM by mass. Clearance readings are normalized by setting initial A_{500} readings to 1. Loss of light scattering in *E* is measured by subtracting normalized A_{500} readings from 1. Leakage measurements are normalized by setting maximal fluorescence readings in the presence of Triton X-100 to 1. Both loss of light scattering and leakage measurements in *E* are scaled such that the lowest light scattering loss or leakage reading is set to 0, and the highest reading is set to 1 (see "Experimental Procedures"). CD readings are normalized to MRE.

In addition, we tested IAPP clearance of POPG and DOPG vesicles, because phosphatidylglycerol is a membrane component that is widely used in the literature (37, 65, 66). Both hIAPP and, albeit less so, rIAPP moderately cleared light scattering from POPG more than that from DOPG, although not to the extent that they cleared POPS light scattering (as summarized in Fig. 1*C*). Both types of IAPP showed a less pronounced effect on DOPG than did α-synuclein (Fig. 1*C*). For all the data shown, α-synuclein, a 140-amino acid protein, was used at a mass per volume equal to that of IAPP, resulting in a 1:74 rather than a 1:20 protein/lipid molar ratio for α-synuclein and therefore a

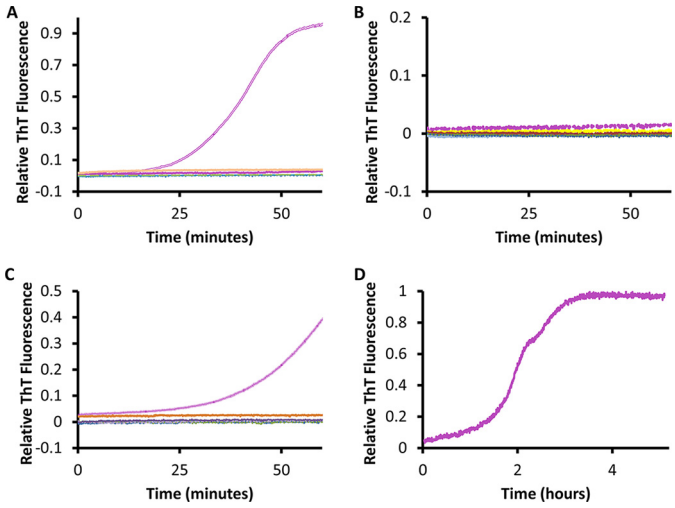

FIGURE 2. **ThT fluorescence of peptide-MLV combinations.** Fluorescence of ThT was measured in the presence of hIAPP and 66:34 POPS/POPC (*magenta double*), hIAPP and 100% POPS (*magenta solid*), α-synuclein and 66:34 POPS/POPC (*turquoise dots*), α-synuclein and 100% POPS (*turquoise solid*), rIAPP and 66:34 POPS/POPC (*green dashes*), or rIAPP and 100% POPS (*light orange solid*) (*A*); hIAPP and 33:67 POPS/POPC (*magenta dashes*), hIAPP and 100% POPC (*deep red solid*), α-synuclein and 33:67 POPS/POPC (*light blue solid*), α-synuclein and 100% POPC (*deep blue dots*), rIAPP and 33:67 POPS/POPC (*yellow solid*), or rIAPP and 100% POPC (*green solid*) (*B*); or hIAPP and 100% POPG (*magenta triple*), hIAPP and 100% DOPG (*light purple dashes*), α-synuclein and 100% POPG (*deep blue solid*), α-synuclein and 100% DOPG (*purple solid*), rIAPP and 100% POPG (*green dots*), or rIAPP and 100% DOPG (*orange solid*) (*C*). ThT readings are normalized by setting the maximal reading for the sample that yielded the largest fluorescence increase (namely, hIAPP and 66:34 POPS/POPC) to 1 so that other readings are recorded as fractions thereof. *D*, example of sigmoidal curve of ThT fluorescence in the presence of hIAPP and 100% POPS over time. Readings are normalized by setting the maximal reading to 1.

TABLE 1

Time points when light scattering reached its minimum (*i.e.* the sample reached maximal clearance) and when scattering began to increase due to protein aggregation

NA means not applicable (light scattering did not significantly decrease/increase within 2 h).

Lipid composition	Time (in minutes) at light scattering minimum/light scattering increase		
	hIAPP	rIAPP	α-Synuclein
100% POPS	20/NA	20/NA	50/NA
66:34 POPS/POPC	10/20	20/NA	60/NA
33:67 POPS/POPC	5/20	NA/NA	NA/NA
100% POPC	NA/NA	NA/NA	NA/NA
100% POPG	30/50	60/NA	60/NA
100% DOPG	10/20	50/NA	60/NA

smaller clearance effect by α-synuclein on POPG in this experiment than in our previously published study, which utilized a 1:20 α-synuclein/POPG molar ratio (52).

Thus far, all clearance assays were conducted using 500 μM phospholipid and 25 μM IAPP. To evaluate whether or not the mechanism behind the observed vesicle clearance involved a cooperative mechanism, we measured the light scattering of 66:34 POPS/POPC MLVs in the presence of hIAPP at a range of different peptide concentrations (while fixing the phospholipid concentration at 500 μM). We observed a sigmoidal rather than linear relationship between hIAPP concentration and vesicle clearance (Fig. 1*E*), suggestive of a cooperative mechanism.

To ensure that the agent that induced vesicle clearance did not consist of protein aggregates, we performed ThT fluorescence assays, which have also been performed extensively in the past on IAPP and α-synuclein under membrane-binding conditions (39, 67, 68). We measured ThT fluorescence in parallel to our 1:20 protein/lipid ratio clearance assays (Fig. 2, *A*–*C*), which corresponded to the highest IAPP concentration tested. We found no misfolding to occur in rIAPP or α-synuclein or in most of our hIAPP measurements under these conditions. We observed misfolding in hIAPP in some cases (as illustrated in Fig. 2*D*, showing ThT fluorescence in the presence of hIAPP and 100% POPS over a longer time course), and in all those cases the increase occurred only after the time frame required for light scattering by vesicles to reach its minimum (where applicable, as listed in Table 1). In addition, leakage (Fig. 5, below) under these conditions began immediately upon addition of IAPP and was at or near completion upon attaining the time frame required for a significant ThT fluorescence increase (Fig. 2ABC).

IAPP Reduces Negatively Charged Giant Vesicles into Smaller Lipidic Structures as Visualized by Fluorescence Microscopy—Our next step was to view the consequences of IAPP-membrane interactions directly. We immobilized GUVs and observed them under fluorescence confocal microscopy. Within 6 s of adding hIAPP, POPS vesicles dissolved into small structures (supplemental video S1 and Fig. 3*A*, *green*), although control POPC vesicles present in the same preparation remained intact (Fig. 3*A*, *blue*, and supplemental video S1). POPS GUVs treated with rIAPP also disbanded into smaller lipidic structures, with POPC remaining intact (Fig. 3*B* and supplemental video S2). Samples were observed for at least 10 min after addition of either variety of IAPP, at which point still no dissolution of POPC vesicles was observed (Fig. 3, *A, panel iv,* and *B, panel iv*).

IAPP Modulates Membrane Architecture to Form Structures of High Curvature as Visualized by EM—Thus far, we have observed that, when added to negatively charged vesicles, α-helical IAPP leads to a population of smaller lipidic structures. To glean more information on the structures formed from affected vesicles, we used negative stain EM to visualize large vesicles before (example of POPS shown in Fig. 4*A*) and after (Fig. 4, *B* and *C*) treatment with IAPP. Both hIAPP (Fig. 4*B*) and rIAPP (Fig. 4*C*) induced formation of smaller vesicles from large ones made of POPS. The size distribution histogram (Fig. 4*D*) for treated and untreated POPS vesicles shows a greater proportion of small vesicles in the presence of either IAPP compared with POPS alone; in particular, <20% of the vesicles counted that were untreated measured under 150 nm in diameter, whereas ~70% of those treated with hIAPP and ~60% of those treated with rIAPP measured under 150 nm.

In addition, we observed tubule formation, another way in which curvature induction can manifest itself, in some IAPP-lipid combinations (Fig. 4, *E*–*G*). However, the result that we detected was not a consistent generation of tubules upon mixing lipids with IAPP but was instead a heterogeneous mix of images across individual EM grids, such that even combinations that led to tubulation showed no tubes in other places on their respective grids (as illustrated in Fig. 4, *H* and *I*). This heterogeneity is in contrast to the stable, consistent tubulation generated by α-synuclein (52, 54). Furthermore, in the 5:95

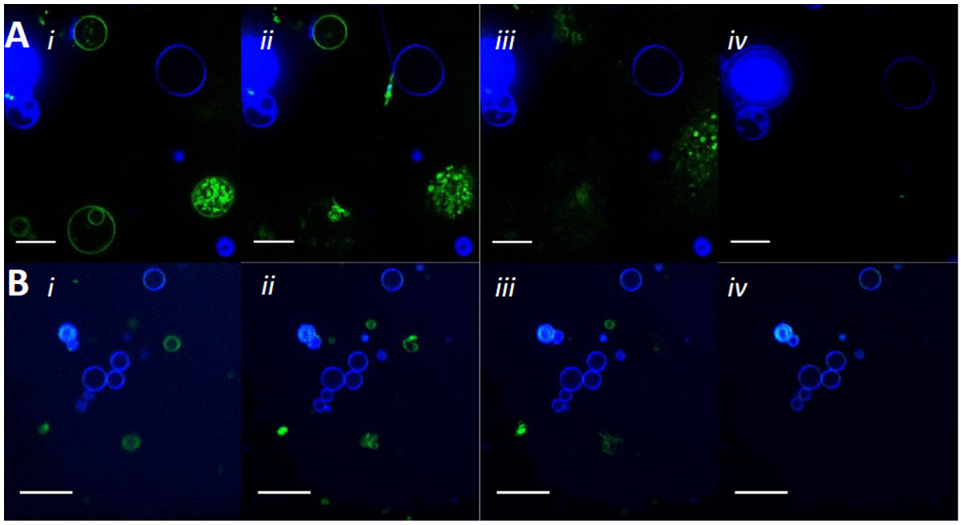

FIGURE 3. **Dissolution of POPS membranes by IAPP visualized directly under fluorescence microscopy.** GUVs composed of 99.2:0.5:0.3 POPS/NBD-PS/biotin-PE (*green*) or of 99.2:0.5:0.3 POPC/Rh-PE/biotin-PE (*blue*) before (*panel i*), immediately after (*panel ii*), 6 s after (*panel iii*), and 10 min after (*panel iv*) treatment with hIAPP (*A*) or rIAPP (*B*). *Scale bar,* 15 μm.

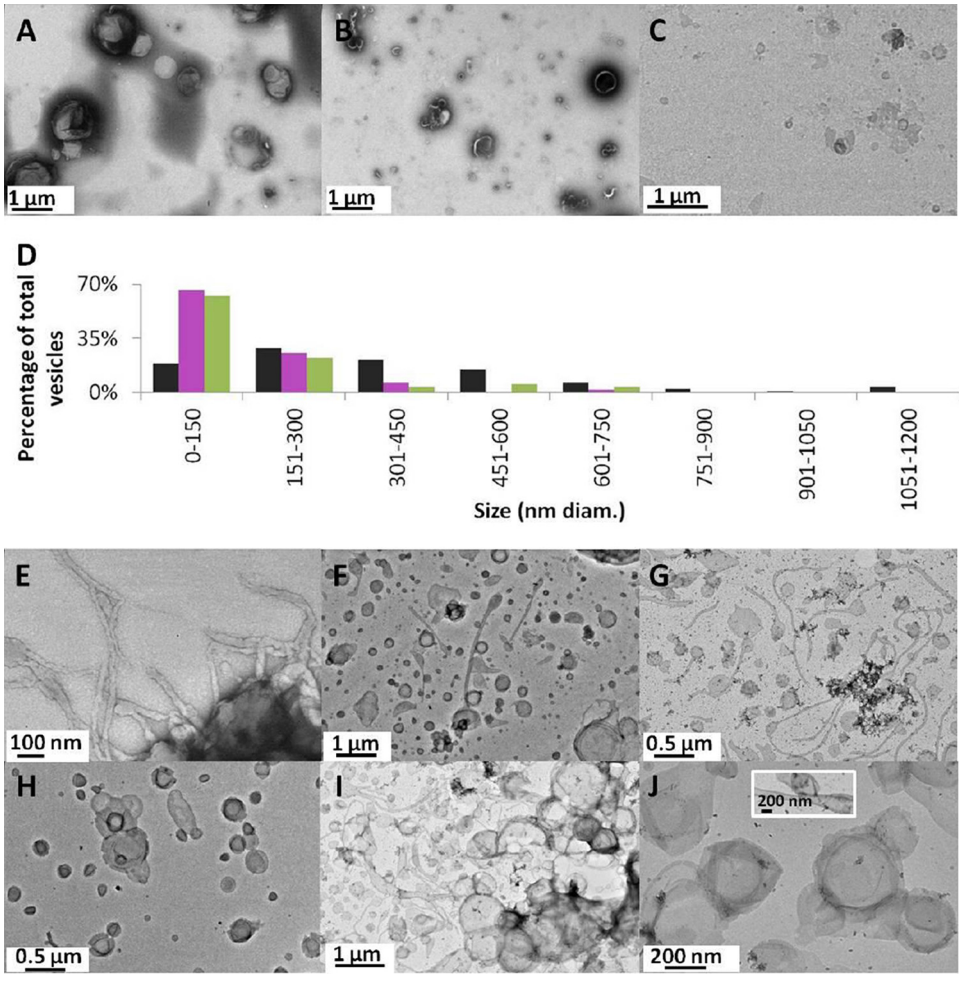

FIGURE 4. **Negative stain EM of the interaction of hIAPP or rIAPP with large vesicles.** POPS was viewed in the absence of peptide (*A*), with hIAPP (*B*), and with rIAPP (*C*). Protein/single phospholipid molar ratios were 1:20. *D*, size distributions of 100% POPS vesicles alone (*black*), with hIAPP (*magenta*), or with rIAPP (*green*). A negligible percentage of vesicles was measured to be over 1200 nm in diameter. DOPG (*E*) was viewed in the presence of hIAPP. Protein/single phospholipid molar ratio was 1:20. Vesicles composed of 20:80 POPS/POPC (*F*) and of 5:95 POPS/POPC (*G*) were viewed in the presence of rIAPP. Protein/single phospholipid molar ratios were 1:180. *H* shows the same 20:80 POPS/POPC sample as in *F*, and *I* shows the same 5:95 POPS/POPC sample as in *G*, with areas of respective grids showing little tubulation. *J*, 5:95 POPS/POPC in the absence of peptide, showing some baseline tubulation (*inset*). The lipidic tubular structures seen in a number of the EM images are distinctly different from protein fibrillar structures, which appear in none of the EM images taken within experimental time frames.

POPS/POPC MLVs in the absence of peptide (Fig. 4*J*), we did observe a small amount of tubulation (Fig. 4*J*, *inset*), which indicates a baseline of spontaneous tubulation in high-POPC content vesicles. Thus, in contrast to higher negative charge conditions, it is more difficult to cleanly conclude that membrane curvature was induced by IAPP at 5% phosphatidylserine content. Also observable in some IAPP-lipid combinations (see, for example, Fig. 4*C*) was the formation of irregularly shaped amorphous structures that resemble neither tubules nor vesicles. These structures might have been a consequence of membrane fragmentation (69).

IAPP Induces Vesicle Leakage in a Charge-dependent Manner—To assess whether the reduction in vesicle size correlated with loss of membrane integrity, we next measured vesicle leakage. IAPP was added to LUVs encapsulating the fluorophore ANTS and its quencher DPX, and ANTS fluorescence was monitored as a measure of membrane leakage. LUVs made up of 66:34 POPS/POPC at a phospholipid concentration of 500 μM leaked up to their respective plateaus within 10 min of addition of 25 μM hIAPP or rIAPP, with the latter being slightly less potent under these conditions (Fig. 5). In both cases, the time frame was faster than that required for clearance of IAPP-treated vesicles of various amounts of POPS to reach its plateau (Fig. 1*A* and Table 1). This time course indicates that vesicle integrity is already breached at the onset of membrane remodeling. Overall, the time course corresponds to those previously observed for α-synuclein and amphiphysin (52). Furthermore, treating 500 μM 66:34 POPS/POPC vesicles with varying concentrations of hIAPP revealed the resulting vesicle leakage to have a nonlinear IAPP dose dependence with a threshold concentration of 2 μM corresponding to a 1:250 protein/single phospholipid molar ratio (Fig. 1*E*), which was similar to the dose dependence of vesicle clearance (Fig. 1*E*). Although neither hIAPP nor rIAPP appreciably caused leakage of 100% POPC-containing LUVs (Fig. 5), 10:90 POPS/POPC-containing LUVs leaked in the presence of hIAPP, whereas rIAPP only caused minor leakage (Fig. 5). Thus, as in the case of the clearance experiments, hIAPP had a stronger effect on membranes, and the difference between the peptides was most pronounced at intermediate lipid charge densities.

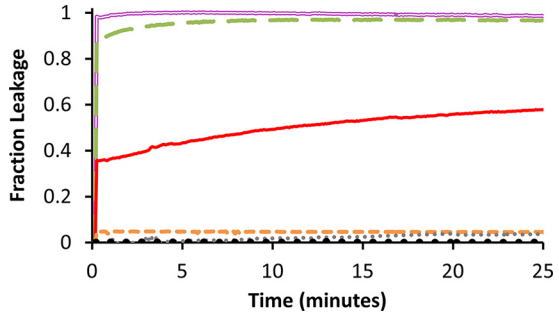

FIGURE 5. **IAPP-induced vesicle leakage.** Leakage was observed for LUVs encapsulating ANTS and its quencher DPX with membranes made of 66:34 POPS/POPC in the presence of hIAPP (*magenta, double line*) or rIAPP (*green, long dashes*); 10:90 POPS/POPC in the presence of hIAPP (*red, solid*) or rIAPP (*orange, short dashes*); or 100% POPC in the presence of hIAPP (*black, large dots*) or rIAPP (*gray, small dots*). Protein/phospholipid molar ratios are 1:20.

IAPP Senses Membrane Curvature under Conditions That Only Moderately Favor Binding—Depending on conditions, some membrane curvature-inducing proteins have been shown to act alternately as sensors (57, 60). To delve into the possible membrane curvature-sensing properties of IAPP, we used CD to quantify the helicity of rIAPP on LUVs and SUVs, which are about 100 and 40 nm in diameter, respectively, and the latter of which is by nature more highly curved. We restricted this part of our study to rIAPP, which does not misfold readily and can thus be more stably investigated by CD over a wide range of conditions.

We measured the CD spectra of rIAPP on LUVs and SUVs consisting of 10:90, 20:80, 33:67, and 66:34 POPS/POPC, using only three-quarters of the lipid molar concentration for SUVs as for LUVs to offset the fact that approximately two-thirds of the phospholipids in SUV membranes, as opposed to about half of the phospholipids in LUV membranes, compose the outer leaflet (70). As an example, spectra from 20:80 POPS/POPC are shown in Fig. 6*A*. rIAPP in the absence of vesicles yields a spectrum that peaks with negative ellipticity at ~200 nm, indicating a mostly random coil structure with only slight helicity. In contrast, the CD spectrum of rIAPP in the presence of 20:80 POPS/POPC SUVs displays negative peaks at 208 and 222 nm, signifying an α-helical structure. rIAPP with LUVs presents a CD spectrum that is intermediate between the other two. The three spectra intersect at a wavelength of 204 nm, an isosbestic point typical of spectra of a peptide transitioning between random coil and helical states. We conclude that, at this composition, the more highly curved vesicles induce more rIAPP to enter the

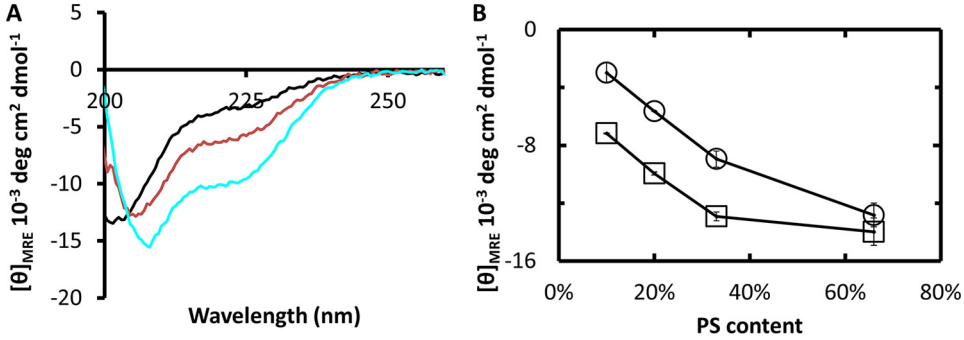

FIGURE 6. **Membrane curvature sensitivity of rIAPP.** *A*, representative MRE spectra for rIAPP alone (*black*) or in the presence of 20:80 POPS/POPC LUVs (*red*) or of SUVs of the same composition (*turquoise*). Spectra intersect at the isosbestic point of 204 nm. *B*, MRE values at 222 nm plotted against POPS content for rIAPP on LUVs (*circles*) and SUVs (*squares*) of different compositions. Each point represents the average of three experiments. *Error bars* represent standard error; $n = 3$. Where *error bars* appear as *horizontal lines*, standard error is too small to be seen as a *vertical line*. Single phospholipid concentration is 2 mM for LUVs and 1.5 mM for SUVs. rIAPP concentration is 25 μM in each case.

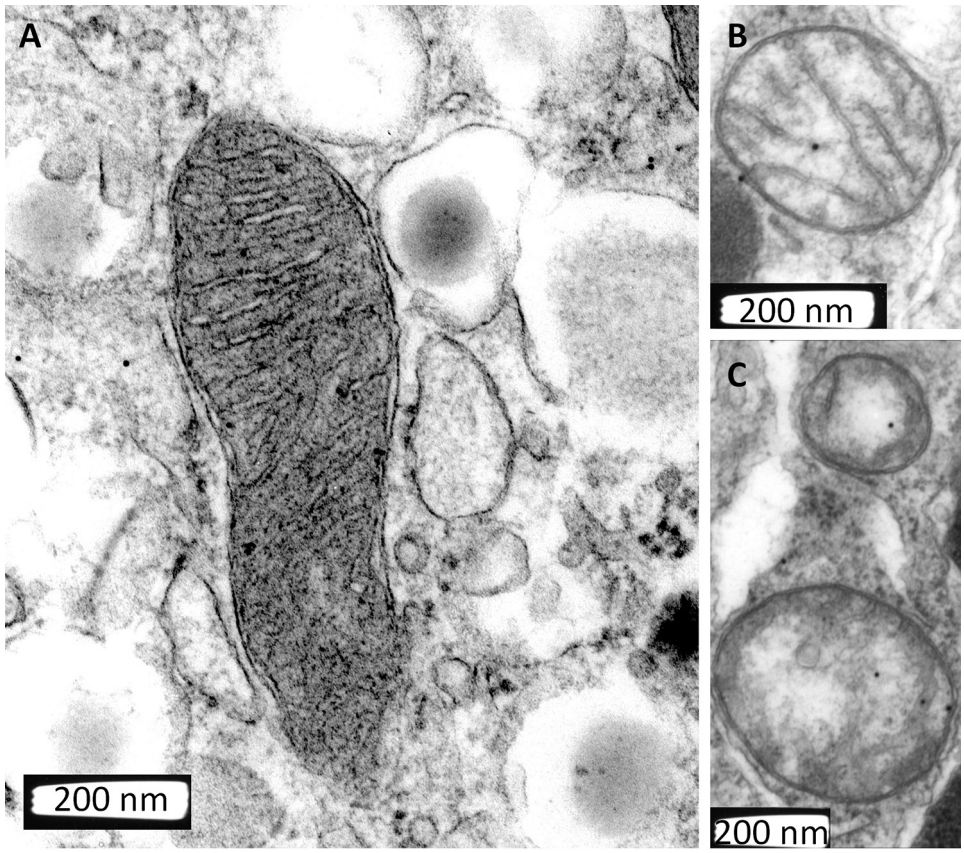

FIGURE 7. **IAPP binding to mitochondria and vesicular structures *in vivo*.** EM images showing immunogold-labeled endogenous IAPP bound chiefly to mitochondria in female mouse islet cells (*A*) and human insulinoma cells (*B* and *C*).

α-helical, and therefore membrane-bound, state. To quantify this difference, we plotted the MRE values at 222 nm as a measure of α-helicity of rIAPP in the presence of LUVs or SUVs of varying POPS content (Fig. 6*B*). MRE values at 222 nm differed substantially between SUVs and LUVs in each case except for 66:34 POPS/POPC, where the values were similar. We conclude that, at low negative charge, α-helicity of rIAPP is dependent upon membrane curvature. Thus, it appears that IAPP acts as a membrane curvature sensor under conditions that limit binding and as a membrane curvature inducer under conditions that strongly favor binding (see under "Discussion").

Having established that IAPP has the ability to sense and/or induce membrane curvature, we next wanted to investigate whether membrane curvature may be a factor in the cellular localization of IAPP. To probe this possibility, we viewed immunogold-labeled endogenous IAPP under EM in mouse pancreatic islet β-cells (Fig. 7*A*) and in cells from an insulinoma removed from a human (Fig. 7, *B* and *C*), and we observed it to bind to the cristae of the inner mitochondrial membrane, as well as other intra- and extracellular vesicular structures. Although our EM images lack the three-dimensional resolution to show that IAPP exclusively interacts with curved membranes, it should be noted that mitochondrial cristae as well as crista-crista junctions are predominantly highly curved, containing extensive tubular as well as bent membranes (71–73). Aside from the physical curvature, mitochondrial cristae are rich in phosphatidylethanolamine and cardiolipin, lipids known to harbor significant amounts of negative spontaneous curvature (74–76). Such spontaneous curvature is the consequence of a low headgroup to acyl chain ratio causing low packing densities in the headgroup region, thereby mimicking the effects of physical curvature. Together, phosphatidylethanolamine and cardiolipin constitute at least half of the phospholipid composition of inner mitochondrial membranes (76), lending these membranes curvature that likely increases IAPP's binding affinity for them.

Discussion

This study sought to uncover the effects of α-helical IAPP on membranes. We detected charge-dependent induction of membrane curvature as a result of IAPP-membrane interactions, leading to the formation of a range of highly curved structures accompanied by disruption of membrane integrity as well as leakage. This effect was strongest for hIAPP, although rIAPP was also capable of inducing membrane curvature. In addition, we observed IAPP to act as a membrane curvature sensor under conditions that limit membrane binding. Our data show IAPP to be α-helical for the duration of this membrane curvature-inducing and -sensing activity.

α-Synuclein, another amyloid protein, has previously been observed to induce membrane curvature in a similar manner (52–55) to the behavior of IAPP in this study. We propose that membrane curvature, whether induced by α-synuclein or by IAPP, is mediated by the wedging of membrane-inserting amphipathic helices. Although both IAPP and α-synuclein induce tubulation and vesiculation of membranes, α-synuclein

has a tendency to generate more stable tubules, whereas tubulation exerted by IAPP is far weaker. This difference between the proteins in the ensuing lipid tubule stability is likely due to the unusually extended helical structure of α-synuclein that is ~140 Å in length (77). We previously noted that the long helical structure of α-synuclein generates a highly anisotropic curvature strain that is ideally suited for stabilizing the anisotropic curvature of tubes (52). In agreement with this notion, we find that the shorter IAPP helix is less capable of stabilizing tubular structures. Regardless of this difference, our data link the membrane curvature-inducing abilities of both proteins to a loss of membrane integrity. Furthermore, we observed amorphous structures that were neither tubular nor vesicular. Those structures could be similar to the protein-lipid complexes previously observed for α-synuclein (55) and could explain the previous finding of membrane fragmentation reported for IAPP (69).

Considering the general prevalence of disruption of membrane integrity by amyloid proteins (78), could the inferred membrane curvature induction mechanism be more general? Amyloid β-peptide and huntingtin have been observed to bind to membranes using the insertion of amphipathic helices (79, 80). This manner of membrane binding is similar to that of IAPP (39–43), and one might expect potential induction of membrane curvature via helical wedges in those proteins as well. Such membrane remodeling could further be facilitated by oligomeric structures that act as delivery vehicles, creating a high local protein density. Additional structural studies are needed to assess utilization of this membrane curvature mechanism by amyloid proteins other than IAPP and α-synuclein.

We tested the hIAPP concentration dependence for two gauges of membrane damage, vesicle leakage and vesicle clearance. The resulting curves (Fig. 1*E*) were sigmoidal and similar to one another, suggesting that leakage and clearance likely occur by related mechanisms. Although leakage measures small openings in the membrane that allow fluorophores to escape, clearance results from major changes in vesicle size. Because the latter can be expected to occur over a longer time frame, this intrinsic difference between measuring leakage and measuring loss of light scattering likely accounts for the steeper increase in leakage observed at intermediate IAPP concentrations (Fig. 1*E*). It should be noted that, although changes in light scattering proceed at a slightly reduced slope relative to leakage, the two measurements still exhibit similar concentration-dependent behavior (Fig. 1*E*). The nonlinearity of both curves indicates that this mechanism is cooperative, an observation in step with previous findings that hIAPP disrupts membrane integrity in a cooperative manner (21, 40). The precise reason for the cooperativity is presently unknown, and future studies will have to show whether increases in concentration simply lead to a critical density of membrane wedges or whether IAPP oligomerization on the membrane is necessary.

Membrane binding by IAPP depends upon membrane curvature (Fig. 6) and charge density (Fig. 1*C*), where a higher density of negative charge in the membrane leads to a stronger driving force for membrane interaction and therefore curvature induction (Figs. 1 and 4). At lower negative charge densities, some membrane remodeling is observed (Fig. 4, *F* and *G*), but under such conditions membrane binding becomes strongly sensitive to membrane curvature (Fig. 6). Thus, with the decrease in driving force for IAPP-membrane interactions due to lower negative charge density comes an increasingly pronounced positive effect on membrane binding originating from the additional spacing between headgroups in more highly curved membranes (Fig. 8*A*), whereas high negative charge densities cause IAPP to insert into membranes without the need for existing membrane curvature, and this insertion induces new membrane curvature (Fig. 8*B*). Therefore, membrane curvature sensing and inducing are likely to be coupled phenomena that depend upon the affinity of IAPP for the membrane, as governed by negative charge density. Our *in vitro* data suggest that hIAPP and rIAPP disrupt membrane integrity by induction of membrane curvature but that hIAPP does so more efficiently, especially in the presence of membranes composed of more modest and physiologically relevant levels of negative charge. This quantitative rather than qualitative difference between hIAPP and rIAPP is consistent with the recent finding that rIAPP can become toxic, but much higher concentrations are required for this peptide (12). The comparatively modest effects of rIAPP on membranes are consistent with prior studies (21, 40, 81). One of these studies found that the His-18 to Arg-18 mutation in rIAPP plays an important role in the differences between rIAPP and hIAPP membrane perturbation (21).

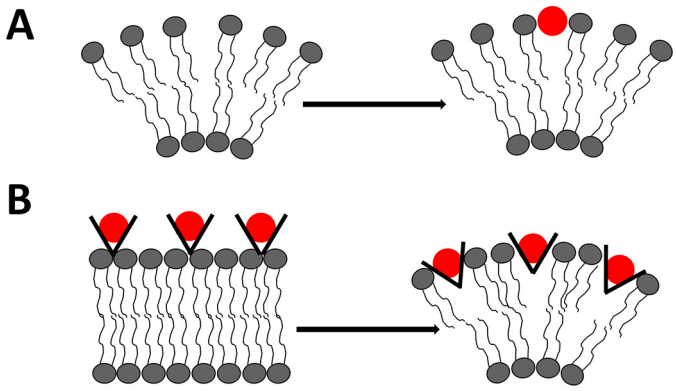

FIGURE 8. **Schematic of relationship between membrane curvature-inducing and curvature-sensing behavior in α-helical IAPP.** *A,* IAPP easily binds, even at low negative charge density, to highly curved membranes by fitting between the spaced headgroups. *B,* at high membrane negative charge, IAPP binds to membranes regardless of local curvature, wedging headgroups apart in planar membranes to force curvature.

Curiously, in β-cells of hIAPP-expressing rodent models of type II diabetes as well as those of humans with type II diabetes, mitochondrial membranes, which are partially negatively charged, are particularly prone to disruption (6). Our *in vivo* EM data (Fig. 7) show human and rat IAPP to localize to mitochondria. Considering that hIAPP is more potent at remodeling membranes, one might expect that hIAPP becomes more disruptive to these membranes than rIAPP. The driving force for such membrane disruption could further be enhanced by increased negative charge density of the mitochondrial lipids or increased local concentrations of hIAPP, possibly by oligomerization. The notion that α-helical hIAPP senses membrane curvature and disturbs the architecture of crista membranes is further supported by the discovery that α-helical IAPP abrogates mitochondrial function (12). Furthermore, other studies showed that α-helical hIAPP oligomers permeabilize pancre-

atic β-cell membranes and cause those cells to lose their normal morphology and viability (82) and that targeting the α-helical form of hIAPP can be protective to cells and membranes (83). The finding that induction of membrane curvature by amyloidogenic proteins results in disruption of membrane integrity and presumably toxicity might ultimately lead to new therapeutic strategies.

Author Contributions—N. C. K., M. A., S. A. J., P. C. B., and R. L. designed the study. N. C. K. designed and performed the experiments shown in Figs. 1, 2, 4, and 6. S. S. designed and performed the experiments shown in Fig. 3 and supplemental videos S1 and S2. M. A. and S. A. J. designed and performed the experiments shown in Fig. 5. P. C. B. designed and performed the experiments shown in Fig. 7. N. M. contributed the microscopy tools for the experiments delineated in Fig. 3 and supplemental videos S1 and S2. N. C. K., S. A. J., P. C. B., and R. L. analyzed the data. N. C. K., S. S., P. C. B., and R. L. wrote the paper. All authors reviewed the results and approved the final version of the manuscript.

Acknowledgments—We thank Alan Okada and Thalia Bajakian for technical assistance.

References

1. Glabe, C. G. (2006) Common mechanisms of amyloid oligomer pathogenesis in degenerative disease. *Neurobiol. Aging* **27,** 570–575
2. Butler, P. C., Chou, J., Carter, W. B., Wang, Y. N., Bu, B. H., Chang, D., Chang, J. K., and Rizza, R. A. (1990) Effects of meal ingestion on plasma amylin concentration in NIDDM and nondiabetic humans. *Diabetes* **39,** 752–756
3. Woods, S. C., Lutz, T. A., Geary, N., and Langhans, W. (2006) Pancreatic signals controlling food intake; insulin, glucagon and amylin. *Philos. Trans. R. Soc. Lond. B Biol. Sci.* **361,** 1219–1235
4. Cooper, G. J., Willis, A. C., Clark, A., Turner, R. C., Sim, R. B., and Reid, K. B. (1987) Purification and characterization of a peptide from amyloid-rich pancreases of type 2 diabetic patients. *Proc. Natl. Acad. Sci. U.S.A.* **84,** 8628–8632
5. Janson, J., Soeller, W. C., Roche, P. C., Nelson, R. T., Torchia, A. J., Kreutter, D. K., and Butler, P. C. (1996) Spontaneous diabetes mellitus in transgenic mice expressing human islet amyloid polypeptide. *Proc. Natl. Acad. Sci. U.S.A.* **93,** 7283–7288
6. Gurlo, T., Ryazantsev, S., Huang, C. J., Yeh, M. W., Reber, H. A., Hines, O. J., O'Brien, T. D., Glabe, C. G., and Butler, P. C. (2010) Evidence for proteotoxicity in beta cells in type 2 diabetes: toxic islet amyloid polypeptide oligomers form intracellularly in the secretory pathway. *Am. J. Pathol.* **176,** 861–869
7. Zhang, S., Liu, H., Chuang, C. L., Li, X., Au, M., Zhang, L., Phillips, A. R., Scott, D. W., and Cooper, G. J. (2014) The pathogenic mechanism of diabetes varies with the degree of overexpression and oligomerization of human amylin in the pancreatic islet beta cells. *FASEB J.* **28,** 5083–5096
8. Burke, K. A., Hensal, K. M., Umbaugh, C. S., Chaibva, M., and Legleiter, J. (2013) Huntingtin disrupts lipid bilayers in a polyQ-length dependent manner. *Biochim. Biophys. Acta* **1828,** 1953–1961
9. Thapa, A., Vernon, B. C., De la Peña, K., Soliz, G., Moreno, H. A., López, G. P., and Chi, E. Y. (2013) Membrane-mediated neuroprotection by curcumin from amyloid-β-peptide-induced toxicity. *Langmuir* **29,** 11713–11723
10. Stefanovic, A. N., Stöckl, M. T., Claessens, M. M., and Subramaniam, V. (2014) α-Synuclein oligomers distinctively permeabilize complex model membranes. *FEBS J.* **281,** 2838–2850
11. Janson, J., Ashley, R. H., Harrison, D., McIntyre, S., and Butler, P. C. (1999) The mechanism of islet amyloid polypeptide toxicity is membrane disruption by intermediate-sized toxic amyloid particles. *Diabetes* **48,** 491–498
12. Magzoub, M., and Miranker, A. D. (2012) Concentration-dependent transitions govern the subcellular localization of islet amyloid polypeptide. *FASEB J.* **26,** 1228–1238
13. Brender, J. R., Lee, E. L., Cavitt, M. A., Gafni, A., Steel, D. G., and Ramamoorthy, A. (2008) Amyloid fiber formation and membrane disruption are separate processes localized in two distinct regions of IAPP, the type-2-diabetes-related peptide. *J. Am. Chem. Soc.* **130,** 6424–6429
14. Brender, J. R., Lee, E. L., Hartman, K., Wong, P. T., Ramamoorthy, A., Steel, D. G., and Gafni, A. (2011) Biphasic effects of insulin on islet amyloid polypeptide membrane disruption. *Biophys. J.* **100,** 685–692
15. Heyl, D. L., Osborne, J. M., Pamarthy, S., Samisetti, S., Gray, A. W., Jayaprakash, A., Konda, S., Brown, D. J., Miller, S. R., Eizadkhah, R., and Milletti, M. C. (2010) Liposome damage and modeling of fragments of human islet amyloid polypeptide (IAPP) support a two-step model of membrane destruction. *Int. J. Pept. Res. Ther.* **16,** 43–54
16. Last, N. B., Rhoades, E., and Miranker, A. D. (2011) Islet amyloid polypeptide demonstrates a persistent capacity to disrupt membrane integrity. *Proc. Natl. Acad. Sci. U.S.A.* **108,** 9460–9465
17. Sparr, E., Engel, M. F., Sakharov, D. V., Sprong, M., Jacobs, J., de Kruijff, B., Höppener, J. W., and Killian, J. A. (2004) Islet amyloid polypeptide-induced membrane leakage involves uptake of lipids by forming amyloid fibers. *FEBS Lett.* **577,** 117–120
18. Engel, M. F., Khemtémourian, L., Kleijer, C. C., Meeldijk, H. J., Jacobs, J., Verkleij, A. J., de Kruijff, B., Killian, J. A., and Höppener, J. W. (2008) Membrane damage by human islet amyloid polypeptide through fibril growth at the membrane. *Proc. Natl. Acad. Sci. U.S.A.* **105,** 6033–6038
19. Westermark, P., Engström, U., Johnson, K. H., Westermark, G. T., and Betsholtz, C. (1990) Islet amyloid polypeptide: pinpointing amino acid residues linked to amyloid fibril formation. *Proc. Natl. Acad. Sci. U.S.A.* **87,** 5036–5040
20. Cao, P., Abedini, A., Wang, H., Tu, L. H., Zhang, X., Schmidt, A. M., and Raleigh, D. P. (2013) Islet amyloid polypeptide toxicity and membrane interactions. *Proc. Natl. Acad. Sci. U.S.A.* **110,** 19279–19284
21. Brender, J. R., Hartman, K., Reid, K. R., Kennedy, R. T., and Ramamoorthy, A. (2008) A single mutation in the nonamyloidogenic region of islet amyloid polypeptide greatly reduces toxicity. *Biochemistry* **47,** 12680–12688
22. Shai, Y. (1999) Mechanism of the binding, insertion and destabilization of phospholipid bilayer membranes by α-helical antimicrobial and cell nonselective membrane-lytic peptides. *Biochim. Biophys. Acta* **1462,** 55–70
23. Jayasinghe, S. A., and Langen, R. (2007) Membrane interaction of islet amyloid polypeptide. *Biochim. Biophys. Acta* **1768,** 2002–2009
24. Almeida, P. F., and Pokorny, A. (2009) Mechanisms of antimicrobial, cytolytic, and cell-penetrating peptides: from kinetics to thermodynamics. *Biochemistry* **48,** 8083–8093
25. Gazit, E., Miller, I. R., Biggin, P. C., Sansom, M. S., and Shai, Y. (1996) Structure and orientation of the mammalian antibacterial peptide cecropin P1 within phospholipid membranes. *J. Mol. Biol.* **258,** 860–870
26. Oren, Z., and Shai, Y. (1998) Mode of action of linear amphipathic α-helical antimicrobial peptides. *Biopolymers* **47,** 451–463
27. Sato, H., and Feix, J. B. (2006) Peptide-membrane interactions and mechanisms of membrane destruction by amphipathic α-helical antimicrobial peptides. *Biochim. Biophys. Acta* **1758,** 1245–1256
28. Chang, W. K., Wimley, W. C., Searson, P. C., Hristova, K., and Merzlyakov, M. (2008) Characterization of antimicrobial peptide activity by electrochemical impedance spectroscopy. *Biochim. Biophys. Acta* **1778,** 2430–2436
29. Matsuzaki, K., Murase, O., Fujii, N., and Miyajima, K. (1995) Translocation of a channel-forming antimicrobial peptide, magainin 2, across lipid bilayers by forming a pore. *Biochemistry* **34,** 6521–6526
30. Langham, A. A., Ahmad, A. S., and Kaznessis, Y. N. (2008) On the nature of antimicrobial activity: a model for protegrin-1 pores. *J. Am. Chem. Soc.* **130,** 4338–4346
31. Allende, D., Simon, S. A., and McIntosh, T. J. (2005) Melittin-induced bilayer leakage depends on lipid material properties: evidence for toroidal pores. *Biophys. J.* **88,** 1828–1837
32. Sengupta, D., Leontiadou, H., Mark, A. E., and Marrink, S. J. (2008) Toroidal pores formed by antimicrobial peptides show significant disorder. *Biochim. Biophys. Acta* **1778,** 2308–2317
33. Bertelsen, K., Dorosz, J., Hansen, S. K., Nielsen, N. C., and Vosegaard,

T. (2012) Mechanisms of peptide-induced pore formation in lipid bilayers investigated by oriented ^{31}P solid-state NMR spectroscopy. *PLoS ONE* **7,** e47745
34. Green, J. D., Kreplak, L., Goldsbury, C., Li Blatter, X., Stolz, M., Cooper, G. S., Seelig, A., Kistler, J., and Aebi, U. (2004) Atomic force microscopy reveals defects within mica supported lipid bilayers induced by the amyloidogenic human amylin peptide. *J. Mol. Biol.* **342,** 877–887
35. Smith, P. E., Brender, J. R., and Ramamoorthy, A. (2009) Induction of negative curvature as a mechanism of cell toxicity by amyloidogenic peptides: the case of islet amyloid polypeptide. *J. Am. Chem. Soc.* **131,** 4470–4478
36. Xu, W., Wei, G., Su, H., Nordenskiöld, L., and Mu, Y. (2011) Effects of cholesterol on pore formation in lipid bilayers induced by human islet amyloid polypeptide fragments: a coarse-grained molecular dynamics study. *Phys. Rev. E Stat. Nonlin. Soft Matter Phys.* **84,** 051922
37. Last, N. B., and Miranker, A. D. (2013) Common mechanism unites membrane poration by amyloid and antimicrobial peptides. *Proc. Natl. Acad. Sci. U.S.A.* **110,** 6382–6387
38. Pannuzzo, M., Raudino, A., Milardi, D., La Rosa, C., and Karttunen, M. (2013) α-Helical structures drive early stages of self-assembly of amyloidogenic amyloid polypeptide aggregate formation in membranes. *Sci. Rep.* **3,** 2781
39. Jayasinghe, S. A., and Langen, R. (2005) Lipid membranes modulate the structure of islet amyloid polypeptide. *Biochemistry* **44,** 12113–12119
40. Knight, J. D., Hebda, J. A., and Miranker, A. D. (2006) Conserved and cooperative assembly of membrane-bound α-helical states of islet amyloid polypeptide. *Biochemistry* **45,** 9496–9508
41. Apostolidou, M., Jayasinghe, S. A., and Langen, R. (2008) Structure of α-helical membrane-bound human islet amyloid polypeptide and its implications for membrane-mediated misfolding. *J. Biol. Chem.* **283,** 17205–17210
42. Patil, S. M., Xu, S., Sheftic, S. R., and Alexandrescu, A. T. (2009) Dynamic α-helix structure of micelle-bound human amylin. *J. Biol. Chem.* **284,** 11982–11991
43. Nanga, R. P., Brender, J. R., Vivekanandan, S., and Ramamoorthy, A. (2011) Structure and membrane orientation of IAPP in its natively amidated form at physiological pH in a membrane environment. *Biochim. Biophys. Acta* **1808,** 2337–2342
44. Peter, B. J., Kent, H. M., Mills, I. G., Vallis, Y., Butler, P. J., Evans, P. R., and McMahon, H. T. (2004) BAR domains as sensors of membrane curvature: the amphiphysin BAR structure. *Science* **303,** 495–499
45. Zimmerberg, J., and Kozlov, M. M. (2006) How proteins produce cellular membrane curvature. *Nat. Rev. Mol. Cell Biol.* **7,** 9–19
46. Campelo, F., McMahon, H. T., and Kozlov, M. M. (2008) The hydrophobic insertion mechanism of membrane curvature generation by proteins. *Biophys. J.* **95,** 2325–2339
47. Löw, C., Weininger, U., Lee, H., Schweimer, K., Neundorf, I., Beck-Sickinger, A. G., Pastor, R. W., and Balbach, J. (2008) Structure and dynamics of helix-0 of the N-BAR domain in lipid micelles and bilayers. *Biophys. J.* **95,** 4315–4323
48. Gallop, J. L., Jao, C. C., Kent, H. M., Butler, P. J., Evans, P. R., Langen, R., and McMahon, H. T. (2006) Mechanism of endophilin N-BAR domain-mediated membrane curvature. *EMBO J.* **25,** 2898–2910
49. Jao, C. C., Hegde, B. G., Gallop, J. L., Hegde, P. B., McMahon, H. T., Haworth, I. S., and Langen, R. (2010) Roles of amphipathic helices and the bin/amphiphysin/rvs (BAR) domain of endophilin in membrane curvature generation. *J. Biol. Chem.* **285,** 20164–20170
50. Cui, H., Mim, C., Vázquez, F. X., Lyman, E., Unger, V. M., and Voth, G. A. (2013) Understanding the role of amphipathic helices in N-BAR domain driven membrane remodeling. *Biophys. J.* **104,** 404–411
51. Ambroso, M. R., Hegde, B. G., and Langen, R. (2014) Endophilin A1 induces different membrane shapes using a conformational switch that is regulated by phosphorylation. *Proc. Natl. Acad. Sci. U.S.A.* **111,** 6982–6987
52. Varkey, J., Isas, J. M., Mizuno, N., Jensen, M. B., Bhatia, V. K., Jao, C. C., Petrlova, J., Voss, J. C., Stamou, D. G., Steven, A. C., and Langen, R. (2010) Membrane curvature induction and tubulation are common features of synucleins and apolipoproteins. *J. Biol. Chem.* **285,** 32486–32493
53. Pandey, A. P., Haque, F., Rochet, J. C., and Hovis, J. S. (2011) α-Synuclein-induced tubule formation in lipid bilayers. *J. Phys. Chem. B* **115,** 5886–5893
54. Mizuno, N., Varkey, J., Kegulian, N. C., Hegde, B. G., Cheng, N., Langen, R., and Steven, A. C. (2012) Remodeling of lipid vesicles into cylindrical micelles by α-synuclein in an extended α-helical conformation. *J. Biol. Chem.* **287,** 29301–29311
55. Varkey, J., Mizuno, N., Hegde, B. G., Cheng, N., Steven, A. C., and Langen, R. (2013) α-Synuclein oligomers with broken helical conformation form lipoprotein nanoparticles. *J. Biol. Chem.* **288,** 17620–17630
56. Boassa, D., Berlanga, M. L., Yang, M. A., Terada, M., Hu, J., Bushong, E. A., Hwang, M., Masliah, E., George, J. M., and Ellisman, M. H. (2013) Mapping the subcellular distribution of α-synuclein in neurons using genetically encoded probes for correlated light and electron microscopy: implications for Parkinson's disease pathogenesis. *J. Neurosci.* **33,** 2605–2615
57. Bhatia, V. K., Madsen, K. L., Bolinger, P. Y., Kunding, A., Hedegård, P., Gether, U., and Stamou, D. (2009) Amphipathic motifs in BAR domains are essential for membrane curvature sensing. *EMBO J.* **28,** 3303–3314
58. Madsen, K. L., Bhatia, V. K., Gether, U., and Stamou, D. (2010) BAR domains, amphipathic helices and membrane-anchored proteins use the same mechanism to sense membrane curvature. *FEBS Lett.* **584,** 1848–1855
59. Cui, H., Lyman, E., and Voth, G. A. (2011) Mechanism of membrane curvature sensing by amphipathic helix containing proteins. *Biophys. J.* **100,** 1271–1279
60. Pranke, I. M., Morello, V., Bigay, J., Gibson, K., Verbavatz, J. M., Antonny, B., and Jackson, C. L. (2011) α-Synuclein and ALPS motifs are membrane curvature sensors whose contrasting chemistry mediates selective vesicle binding. *J. Cell Biol.* **194,** 89–103
61. Ouberai, M. M., Wang, J., Swann, M. J., Galvagnion, C., Guilliams, T., Dobson, C. M., and Welland, M. E. (2013) α-Synuclein senses lipid packing defects and induces lateral expansion of lipids leading to membrane remodeling. *J. Biol. Chem.* **288,** 20883–20895
62. Der-Sarkissian, A., Jao, C. C., Chen, J., and Langen, R. (2003) Structural organization of α-synuclein fibrils studied by site-directed spin labeling. *J. Biol. Chem.* **278,** 37530–37535
63. Angelova, M. I., Soléau, S., Méléard, P., Faucon, J. F., and Bothorel, P. (1992) Preparation of giant vesicles by external AC electric fields. Kinetics and applications. *Progr. Colloid Polym. Sci.* **89,** 127–131
64. O'Brien, T. D., Butler, A. E., Roche, P. C., Johnson, K. H., and Butler, P. C. (1994) Islet amyloid polypeptide in human insulinomas. Evidence for intracellular amyloidogenesis. *Diabetes* **43,** 329–336
65. Brender, J. R., Heyl, D. L., Samisetti, S., Kotler, S. A., Osborne, J. M., Pesaru, R. R., and Ramamoorthy, A. (2013) Membrane disordering is not sufficient for membrane permeabilization by islet amyloid polypeptide: studies of IAPP(20–29) fragments. *Phys. Chem. Chem. Phys.* **15,** 8908–8915
66. Caillon, L., Lequin, O., and Khemtémourian, L. (2013) Evaluation of membrane models and their composition for islet amyloid polypeptide-membrane aggregation. *Biochim. Biophys. Acta* **1828,** 2091–2098
67. Knight, J. D., and Miranker, A. D. (2004) Phospholipid catalysis of diabetic amyloid assembly. *J. Mol. Biol.* **341,** 1175–1187
68. Zhu, M., Li, J., and Fink, A. L. (2003) The association of α-synuclein with membranes affects bilayer structure, stability, and fibril formation. *J. Biol. Chem.* **278,** 40186–40197
69. Brender, J. R., Dürr, U. H., Heyl, D., Budarapu, M. B., and Ramamoorthy, A. (2007) Membrane fragmentation by an amyloidogenic fragment of human islet amyloid polypeptide detected by solid-state NMR spectroscopy of membrane nanotubes. *Biochim. Biophys. Acta* **1768,** 2026–2029
70. Gennis, R. B. (1989) *Biomembranes: Molecular Structure and Function*, pp. 80–83, Springer-Verlag, New York
71. Perkins, G., Renken, C., Martone, M. E., Young, S. J., Ellisman, M., and Frey, T. (1997) Electron tomography of neuronal mitochondria: three-dimensional structure and organization of cristae and membrane contacts. *J. Struct. Biol.* **119,** 260–272
72. Frey, T. G., Renken, C. W., and Perkins, G. A. (2002) Insight into mitochondrial structure and function from electron tomography. *Biochim. Biophys. Acta* **1555,** 196–203
73. Zerbes, R. M., van der Klei, I. J., Veenhuis, M., Pfanner, N., van der Laan, M., and Bohnert, M. (2012) Mitofilin complexes: conserved organizers of

mitochondrial membrane architecture. *Biol. Chem.* **393,** 1247–1261
74. Rustenbeck, I., Matthies, A., and Lenzen, S. (1994) Lipid composition of glucose-stimulated pancreatic islets and insulin-secreting tumor cells. *Lipids* **29,** 685–692
75. Horvath, S. E., and Daum, G. (2013) Lipids of mitochondria. *Prog. Lipid Res.* **52,** 590–614
76. Daum, G., and Vance, J. E. (1997) Import of lipids into mitochondria. *Prog. Lipid Res.* **36,** 103–130
77. Jao, C. C., Hegde, B. G., Chen, J., Haworth, I. S., and Langen, R. (2008) Structure of membrane-bound α-synuclein from site-directed spin labeling and computational refinement. *Proc. Natl. Acad. Sci. U.S.A.* **105,** 19666–19671
78. Relini, A., Marano, N., and Gliozzi, A. (2014) Probing the interplay between amyloidogenic proteins and membranes using lipid monolayers and bilayers. *Adv. Colloid Interface Sci.* **207,** 81–92
79. Terzi, E., Hölzemann, G., and Seelig, J. (1997) Interaction of Alzheimer β-amyloid peptide(1–40) with lipid membranes. *Biochemistry* **36,** 14845–14852
80. Atwal, R. S., Xia, J., Pinchev, D., Taylor, J., Epand, R. M., and Truant, R. (2007) Huntingtin has a membrane association signal that can modulate huntingtin aggregation, nuclear entry and toxicity. *Hum. Mol. Genet.* **16,** 2600–2615
81. Williamson, J. A., and Miranker, A. D. (2007) Direct detection of transient α-helical states in islet amyloid polypeptide. *Protein Sci.* **16,** 110–117
82. Bram, Y., Frydman-Marom, A., Yanai, I., Gilead, S., Shaltiel-Karyo, R., Amdursky, N., and Gazit, E. (2014) Apoptosis induced by islet amyloid polypeptide soluble oligomers is neutralized by diabetes-associated specific antibodies. *Sci. Rep.* **4,** 4267
83. Kumar, S., Schlamadinger, D. E., Brown, M. A., Dunn, J. M., Mercado, B., Hebda, J. A., Saraogi, I., Rhoades, E., Hamilton, A. D., and Miranker, A. D. (2015) Islet amyloid-induced cell death and bilayer integrity loss share a molecular origin targetable with oligopyridylamide-based α-helical mimetics. *Chem. Biol.* **22,** 369–378

VIDEO LEGENDS

VIDEO S1. Fluorescence microscopy video showing POPS membrane dissolution by hIAPP. GUVs composed of 99.2:0.5:0.3 POPS/NBD-PS/biotin-PE (green) or of 99.2:0.5:0.3 POPC/Rh-PE/biotin-PE (blue) were treated with hIAPP resulting in a protein/single phospholipid molar ratio estimated to lie between 1:2.5 and 1:5. Only the POPS GUVs were reduced into smaller lipidic structures, while the POPC GUVs remained intact. Thirty-five seconds are shown; two frames were recorded per second with both channels being recorded simultaneously, while the movie proceeds at a speed of seven frames per second.

VIDEO S2. Fluorescence microscopy video showing POPS membrane dissolution by rIAPP. GUVs composed of 99.2:0.5:0.3 POPS/NBD-PS/biotin-PE (green) or of 99.2:0.5:0.3 POPC/Rh-PE/biotin-PE (blue) were treated with rIAPP resulting in a protein/single phospholipid molar ratio estimated to lie between 1:2.5 and 1:5. Only the POPS GUVs were reduced into smaller lipidic structures, while the POPC GUVs remained intact. Twelve seconds are shown; two frames were recorded per second with both channels being recorded simultaneously, while the movie proceeds at a speed of seven frames per second.

Molecular Biophysics:

Membrane Curvature-sensing and Curvature-inducing Activity of Islet Amyloid Polypeptide and Its Implications for Membrane Disruption

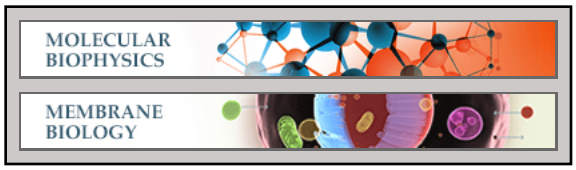

Natalie C. Kegulian, Shalene Sankhagowit, Melania Apostolidou, Sajith A. Jayasinghe, Noah Malmstadt, Peter C. Butler and Ralf Langen

J. Biol. Chem. 2015, 290:25782-25793.
doi: 10.1074/jbc.M115.659797 originally published online August 17, 2015